Measurement of the induced pseudoscalar coupling using radiative muon capture on hydrogen

D. H. Wright,[1] S. Ahmad,[2,*] D. S. Armstrong,[3] G. Azuelos,[1,4] W. Bertl,[5] M. Blecher,[6] C. Q. Chen,[1] P. Depommier,[4] B. C. Doyle,[7,2] T. von Egidy,[1,†] T. P. Gorringe,[7] P. Gumplinger,[1] M. D. Hasinoff,[2] D. Healey,[1] G. Jonkmans,[4,‡] A. J. Larabee,[2,§] J. A. Macdonald,[1] S. C. McDonald,[8,‖] M. Munro,[8] J.-M. Poutissou,[1] R. Poutissou,[1] B. C. Robertson,[9] D. G. Sample,[2] E. Saettler,[2,‡] C. N. Sigler,[6] G. N. Taylor,[8] and N. S. Zhang[2]

[1]*TRIUMF, Vancouver, British Columbia, Canada V6T 2A3*

[2]*University of British Columbia, Vancouver, British Columbia, Canada V6T 1Z1*

[3]*College of William and Mary, Williamsburg, Virginia 23187*

[4]*Université de Montréal, Montréal, Quebec, Canada H3C 3J7*

[5]*Paul Scherrer Institut, CH-5232 Villigen, Switzerland*

[6]*Virginia Polytechnic Institute and State University, Blacksburg, Virginia 24060*

[7]*University of Kentucky, Lexington, Kentucky 40506*

[8]*University of Melbourne, Parkville, Victoria, Australia 3052*

[9]*Queen's University, Kingston, Ontario, Canada K7L 3N6*

(Received 8 July 1997)

The photon energy spectrum from the elementary process $\mu^- p \to \nu_\mu n \gamma$ was measured using a photon pair-spectrometer at the TRIUMF cyclotron. Various sources of backgrounds are discussed in detail and evaluated. From the final spectrum the partial branching ratio R_γ and the pseudoscalar coupling g_p were extracted. The values obtained are $R_\gamma(k>60\ \text{MeV}) = (2.10 \pm 0.21) \times 10^{-8}$ and $g_p(q^2 = -0.88 m_\mu^2) = (9.8 \pm 0.7 \pm 0.3) g_a(0)$, respectively. The first error is the quadrature sum of statistical and systematic errors, while the second error is due to the uncertainty in λ_{op}, the transition rate of the $p\mu p$ molecule from ortho to para states. This measurement of g_p, the most precise to date, agrees with all but one of the previous measurements. However it is 1.46 times the value predicted by the partially conserved axial current hypothesis and pion pole dominance. [S0556-2813(98)03601-2]

PACS number(s): 23.40.Bw, 11.40.Ha, 13.60.−r, 14.20.Dh

I. INTRODUCTION

Muon capture provides a powerful, weakly interacting probe of the proton's structure. The momentum transfer values typical in radiative muon capture correspond to distances of the order of 2 fm, thus yielding information about the outer part of the pion cloud. This information is contained in the weak form factors induced by the strong interaction of the hadrons. The pseudoscalar form factor, which is the subject of this report, is assumed to be dominated by a pole at the pion mass. Radiative muon capture provides momentum transfer values close to the pion pole, thereby allowing a sensitive test of this assumption. Hence a study of the radiative muon capture rate on the proton may allow the most precise determination of the pseudoscalar coupling. A brief report of the first observation of radiative muon capture on H has already been published [1]. The present report is a detailed description of the experiment and the methods by which the pseudoscalar coupling was extracted. Additional details can be found in Refs. [2,3].

II. THEORY

The standard model describes weak interactions at the quark-lepton level in terms of a pure *V-A* coupling. For purely leptonic interactions this is sufficient but for hadron-lepton interactions, the quarks are not free but confined, leading to complex hadron structure. In the absence of a workable, fundamental theory of hadronic structure, the weak interaction at the hadron-lepton level must be described phenomenologically in terms of form factors. The vector and axial-vector form factors modify the basic electroweak interaction. Four additional ''induced'' form factors may also be present [4]. Hence the operator of the Lorentz invariant hadronic current has a form $V_\lambda - A_\lambda$ which consists of two parts [5]:

$$V_\lambda = g_v(q^2)\gamma_\lambda + i g_m(q^2)\sigma_{\lambda\nu}\frac{q^\nu}{2M} + g_s(q^2)\frac{q_\lambda}{m_l}, \tag{1}$$

$$A_\lambda = g_a(q^2)\gamma_\lambda\gamma_5 + g_p(q^2)\frac{q_\lambda}{m_l}\gamma_5 + i g_t(q^2)\sigma_{\lambda\nu}\gamma_5\frac{q^\nu}{2M}. \tag{2}$$

Here m_l is the lepton mass and M is the nucleon mass. The nucleon form factors g are functions of the momentum transfer squared q^2. The four-momentum transfer q_λ is given by $n_\lambda - p_\lambda$, where n and p are the four-momenta of the neutron

*Present address: M.D. Anderson Cancer Center, University of Texas, Houston, TX 77030.

†Present address: Technische Universität München, D-85748, Garching, Germany.

‡Present address: Physics and Astronomy Department, Laurentian University, Sudbury, Ontario, Canada P3E 2C6.

§Present address: Physics Department, University of Texas, El Paso, TX 79968.

‖Present address: Physics Department, University of California, Los Angeles, CA 90095.

and proton, respectively. These form factors are real provided that time reversal invariance holds. The vector and weak magnetism form factors $g_v(q^2)$ and $g_m(q^2)$ are related by the conservation of the weak vector current (CVC) to the nucleon's electromagnetic form factors [6] which are well measured up to large momentum transfer by electron scattering. At low momentum transfer, $g_m(q^2)$ has been measured using β decay [7]. G-parity invariance requires that the tensor $g_t(q^2)$ and scalar $g_s(q^2)$ form factors both vanish. Their current values, $g_t(q^2)=-0.06\pm0.49$ [8] and $g_s(q^2=0)=-0.4\pm2.3$ [9], are consistent with the absence of such second-class currents. The axial-vector form factor $g_a(q^2=0)=1.2601\pm0.0025$ is well known from neutron β decay [10]. Its q^2 dependence is determined by pion electroproduction [11–13] and quasielastic neutrino scattering [14]. The remaining form factor, the pseudoscalar $g_p(q^2)$ is not as well known.

The q^2 dependence of g_p has recently been predicted using the chiral Ward identities of QCD and heavy-baryon chiral perturbation theory [15]:

$$g_p(q^2)=\frac{2m_\mu g_{\pi NN}F_\pi}{m_\pi^2-q^2}-\frac{1}{3}g_a(0)m_\mu M r_a^2. \tag{3}$$

Here, M is the nucleon mass, r_a^2 is the mean square nucleon radius in the axial nucleon form factor, F_π is the pion decay constant, and $g_{\pi NN}$ is the pion-nucleon coupling constant. The same result was derived much earlier using the partially conserved axial current hypothesis (PCAC) [16,17]. Following the calculation of Ref. [15] which uses the most recent values of F_π, $g_{\pi NN}$, and r_a, expression (3) gives the predicted value

$$g_p(q^2=-0.88m_\mu^2)=6.7g_a(0)=8.44\pm0.23 \tag{4}$$

at the fixed momentum transfer of ordinary muon capture (OMC). By convention, when g_p is referred to as a coupling constant, it is actually the form factor $g_p(q^2)$ evaluated at the OMC momentum transfer. The precision of this prediction far exceeds that of any previous experiment, the most precise of which [18] has a 40% error. By comparison, the present experiment has resulted in a precision of 10%.

Previous measurements of g_p [18–24] have used ordinary muon capture $\mu^- p\rightarrow\nu_\mu n$, in which q^2 is fixed at $-0.88m_\mu^2$. While OMC offers a larger momentum transfer and therefore much greater sensitivity to g_p than, for example, β decay, q^2 is still far from the pion pole and a 4% rate measurement yields a 40% uncertainty in g_p [18]. Combining many different OMC results yields only 25% precision [18]. A more recent experiment [13] used pion electroproduction to deduce g_p at several q^2 values further from the pion pole ($q^2=m_\pi^2$). In this case the polelike behavior of $g_p(q^2)$ was verified.

In radiative muon capture (RMC), $\mu^- p\rightarrow\nu_\mu n\gamma$, q^2 is variable and can be much closer to the pion pole, up to $q^2=m_\mu^2$ at maximum photon energy ($k\sim100$ MeV). The resulting contribution of g_p to RMC is more than three times its contribution to the OMC amplitude so that a 20% change in g_p results in a 17 (3)% change in the RMC (OMC) rates. This long known, promising sensitivity to g_p is offset by the very small branching ratio in hydrogen of order 10^{-8}. Due to this small probability and the many potentially large background sources no previous measurement has been attempted. RMC has been measured many times in nuclei [25] where the branching ratio is much larger than in H. However, the interpretation of the results in terms of g_p is clouded by nuclear structure effects and the possible renormalization of the weak form factors in nuclei.

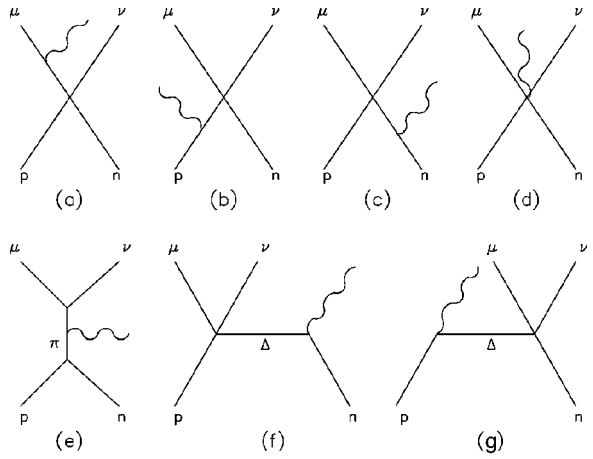

FIG. 1. Feynman diagrams for RMC on H. See text for discussion.

RMC on hydrogen was first calculated in 1957 [26]. Opat [27] was the first to include the hyperfine effects in the singlet and triplet μp atomic states and in the doublet ortho $[p\mu p]$ molecular state. The most recent calculation of Beder and Fearing [28,29] is a relativistic approach based on the tree-level diagrams shown in Fig. 1. Diagrams (a), (b), and (c) represent the photon coupling to the charge and magnetic moments of the initial and final state particles. Diagram (d) is a gauge term. Diagram (e) represents radiation from the internal pion in the diagram responsible for g_p. Diagrams (f) and (g) represent the contribution of Δ excitations.

For the case of muons captured in a liquid hydrogen target, muonic molecular effects must also be considered. The measured RMC rate will then be the weighted sum of the rates in each of the singlet and triplet atomic and ortho and para molecular states, with the weights determined by measured transition rates from state to state. All rates to and from the atomic and molecular muonic hydrogen states are well known except for λ_{op}, the rate at which the ortho $p\mu p$ molecule decays to the para state. Its measured value [18] is $(4.1\pm1.4)\times10^4\ \mathrm{s}^{-1}$, which is smaller than the theoretical prediction $(7.1\pm1.2)\times10^4\ \mathrm{s}^{-1}$ [30]. Fortunately the RMC rate is not strongly dependent on λ_{op}.

III. EXPERIMENTAL SETUP

The very small branching ratio of RMC on hydrogen ($\sim10^{-8}$) places very stringent requirements on any experiment designed to measure it. High muon flux, a very pure hydrogen target, large detector solid angle, reasonable photon energy resolution, and efficient background rejection are all required. The present experiment was performed by stopping a pure, negatively charged muon beam in a liquid hydrogen target. Liquid H_2, rather than high-density gas, was

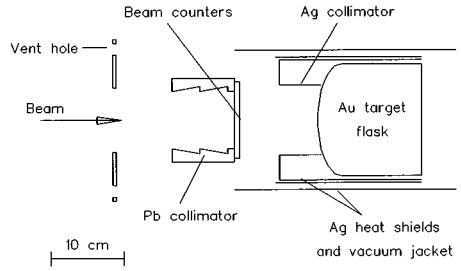

FIG. 2. Liquid hydrogen target and collimator arrangement.

chosen in order to stop nearly all incident muons in the target, thus increasing the count rate for the rare RMC process. Photons from the target were detected in a cylindrical drift chamber pair spectrometer which incorporated a charged-particle veto of electrons from muon decay. Good energy resolution allowed background photons arising from the bremsstrahlung of muon decay electrons to be eliminated from the signal energy range 60–100 MeV. The use of a drift chamber to detect converted photons insured insensitivity to the large background of neutrons from ordinary muon capture. Backgrounds from cosmic-ray-induced photons were rejected in part by an active veto consisting of planar wire chambers and plastic scintillators which surrounded the spectrometer.

The M9A channel at TRIUMF [31] provided muon and pion beams for the experiment. These beams were produced by a primary beam of 500-MeV protons, with a typical current between 100 and 140 μA, striking a 10-cm Be production target. The beam had a macroscopic duty factor of 99% and a microstructure due to the cyclotron rf consisting of a 5-ns pulse every 43.3 ns. Negative muons of 63 MeV/c at a typical rate of 6.5×10^5 s^{-1} with $\delta P/P=10\%$ were counted by a stack of four plastic scintillation counters each 1.6-mm thick and located 12 cm upstream of the front face of the target flask. Electron and pion contaminations were reduced to $e/\mu=5\times10^{-2}$ and $\pi/\mu=2\times10^{-4}$ by an rf separator [32] about 10 m upstream of the hydrogen target. Beams of positive muons for background studies were provided by reversing the channel polarity. By retuning the channel and separator, 81 MeV/c π^- beams were produced for energy calibration and acceptance measurements. In this case the typical beam composition was 96% π^-, 3% e^-, and 1% μ^-. Pulse heights in the beam counters were used offline to further reduce the effects of beam contaminants.

Muons and pions were stopped in 2.7 liters of chemically pure, isotopically separated liquid $^1H_2$. The protium was contained in a thin-walled gold vessel 15-cm long and 16 cm in diameter which was placed at the geometric center of the pair spectrometer. Because the probability of RMC varies roughly as Z^4 and because muons in μH atoms are easily transferred to heavier, contaminant nuclei, great care was taken to avoid chemical impurities. A low concentration of deuterium was also necessary to reduce the rate of muon catalyzed fusion, $p\mu d\rightarrow\mu^3$He, which causes a background from RMC on ^{3}He. To prevent loss and maintain purity, a gas recycling system [33] was developed for use with this target. A schematic diagram of the target and beam collimation system is shown in Fig. 2 and details of its construction

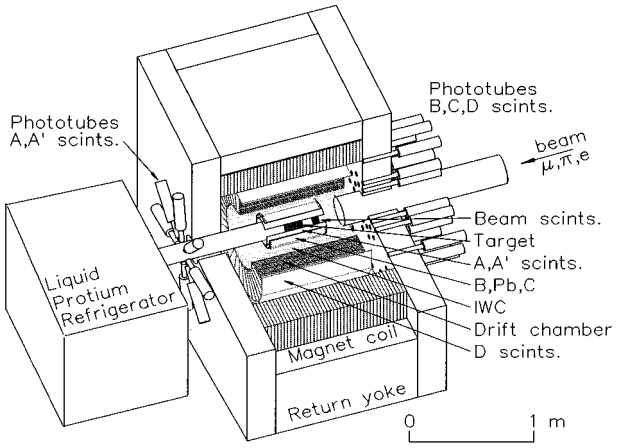

FIG. 3. The RMC pair spectrometer at TRIUMF.

are given elsewhere [34].

Photons were converted to e^+e^- pairs in a 1.08-mm thick, dodecahedral lead sheet surrounding the target at a mean radius of 157 mm. The pairs were then momentum analyzed in a cylindrical pair spectrometer [34] which is shown in Fig. 3. The spectrometer consisted of two concentric, cylindrical chambers, which together provided charged-track reconstruction in three dimensions. The inner chamber (IWC), with a radius of 270 mm, was placed outside of and concentric with the Pb converter. It was a dual-coordinate cylindrical proportional chamber which provided x, y, and z coordinates for a single point on each track passing through it.

The outer chamber (DC) was a large volume cylindrical drift chamber with inner and outer radii of 302 and 580 mm, respectively, and consisted of four superlayers of drift cells. Layers 1, 2, and 4 were axial and provided x,y coordinates for tracks while layer 3, which was stereo, provided z coordinates. The chambers were enclosed within a magnet coil and return yoke which provided a uniform axial field of 0.24 T parallel to both the beam axis and the spectrometer axis. Combining coordinates from both chambers resulted in a spatial resolution for single tracks of 140 μm in x,y and 400 μm in z. The active region of the DC defined the solid angle subtended by the spectrometer at the target center to be $\sim3\pi$ sr. The large solid angle combined with a photon conversion efficiency of about 10% yielded a large average acceptance for photons in the energy range 60 to 100 MeV. As discussed below, this acceptance was measured using the known photon spectrum of pions stopping in hydrogen.

The chamber readout was triggered by a set of azimuthally segmented, concentric layers of plastic scintillator panels labeled A, A', B, C, and D in order of increasing radius. The A and A' counters were located immediately outside of the target while the B counters were located just inside the Pb converter. Their purpose was to veto charged particles originating in the target. The C counters, immediately outside of the Pb converter, and the D counters, just outside the DC, provided pattern information on events in the chambers which was used in the first level trigger. In a typical converted photon event a single C counter and one or two nonadjacent D counters would fire but no A, A', or B counters

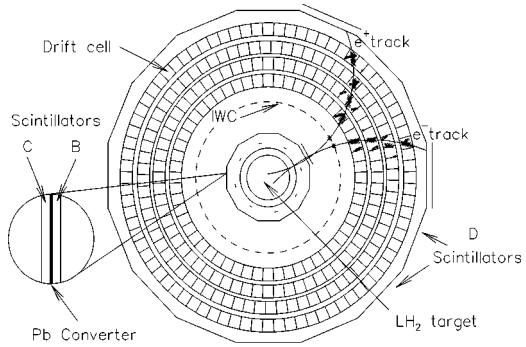

FIG. 4. *X-Y* view of converted photon event. Extra lines parallel to the scintillator panels indicate which C and D counters fired during the event. Six instrumented sense wires are located along the vertical midplane of each drift cell.

would fire. Such an event was accepted by the primary trigger condition

$$\overline{\Sigma(A+A')}\cdot\overline{\Sigma B}\cdot\Sigma C\cdot\geqslant 1D. \tag{5}$$

Higher-level trigger conditions were placed on events by comparing combinations of C and D counter hits to preset patterns stored in programmable logic modules. In addition, crude pattern recognition was performed by recording the number of cells hit in each layer of the DC [35] and accepting only those events having hit distributions consistent with e^+e^- pairs. An xy view of a typical photon event is shown in Fig. 4.

For an incident muon rate of 6×10^5 s^{-1} the primary trigger rate [Eq. (5)] was about 1000 s^{-1}. The higher level conditions discussed above reduced the rate of events written to tape to about 100 s^{-1}. A complete discussion of the trigger is given elsewhere [34].

IV. BACKGROUND REDUCTION METHODS

The photon spectrum from RMC extends from 0 to $\sim$100 MeV and is susceptible to several backgrounds which are described in this section. A quantitative discussion of the actual background subtractions is given in Sec. V.

The small pion contamination remaining in the beam after rf separation gives rise to a potentially dangerous background since each negative pion produces photons from charge exchange or capture:

$$\pi^-+p\rightarrow\pi^0+n\ \ (59.8\%), \tag{6}$$

$$\hookrightarrow\gamma+\gamma+n\ \ (k\sim55-83\ \ \text{MeV}), \tag{7}$$

$$\pi^-+p\rightarrow\gamma+n\ \ (39.3\%,k\sim129\ \ \text{MeV}). \tag{8}$$

Although these pion-induced photons are $\sim10^7$ times more plentiful than RMC photons, they are prompt and can be efficiently vetoed by timing and pulse-height cuts.

The largest irreducible photon background is due to muon decay with a subsequent (outer) bremsstrahlung of the decay electron

$$\mu^-\rightarrow e^-\overline{\nu_e}\nu_\mu \tag{9}$$

$$\hookrightarrow e^-+\gamma \tag{10}$$

and from inner bremsstrahlung

$$\mu^-\rightarrow e^-\overline{\nu_e}\nu_\mu\gamma. \tag{11}$$

Since 99.9% of muons stopping in liquid hydrogen decay before they can be captured, bremsstrahlung represents a copious source of photons with a maximum energy of $m_\mu/2$. The RMC signal at lower energies is therefore insignificant compared to this background. However, the spectrometer energy resolution, $\sim$11% full width at half maximum (FWHM), was sufficient to eliminate most of this background for photon energies above 60 MeV. Leakage into the RMC region due to resolution effects was determined by tuning the beam for μ^+. These can only decay so that a properly normalized subtraction of the μ^+ photon spectrum from the μ^- photon spectrum removed the leakage events. This subtraction was corrected for the fact that positrons from μ^+ decay can produce photons from annihilation-in-flight, whereas the electrons from μ^- decay cannot.

Photons can also be produced by cosmic rays and beam-related backgrounds. Two additional layers of scintillators and drift chambers placed outside the magnet yoke were used to veto cosmic ray events in software. The beam-related background was measured extensively under experimental conditions when the beam was off and when the secondary beam was magnetically diverted, just upstream of the separator, to the adjacent M9B channel.

For muon stopping rates typical of this experiment, there were often more than one muon in the target at a time. Due to the finite memory time of the drift chamber single particle tracks related to different muon decays at somewhat different times could appear superimposed in the same event, imitating a converted photon. However, the trigger counter time signals, which were read out with multihit TDCs, allowed the identification of such spurious near coincidences.

RMC occurred on the gold flask containing the liquid H and on the nearby silver heat shield/collimator much more rapidly than on H ($\sigma\sim Z^4$), creating a potentially huge background. The first step in reducing this background was to design a target flask large enough so that very few muons stop near the walls. Au was chosen for the flask material because it can be made into a very pure thin-walled container. Since the disappearance times for μ^- in Au and Ag (73 and 89 ns) are short compared to that in H (2195 ns), it was possible to wait until nearly all photons from Au and Ag had traversed the spectrometer before selecting any events. Therefore events occurring within 365 ns ($5\tau_{\text{Au}}$) following the last μ^- stop were removed in software. A fit to the uncut time spectrum for $E_\gamma>$ 60 MeV, enabled a determination of the fraction of this background which occurred more than 365 ns after a μ^- stop.

The presence of deuterium or heavy element impurities in liquid hydrogen would also be a serious background source. The various pathways open to a μ^- in liquid H_2 when impurities are present are illustrated in Fig. 5. In liquid the μ^- is rapidly captured into the singlet atomic state. This small neutral system will quickly form a $p\mu p$ molecule, mainly in the ortho state, which can decay to the para state. RMC can proceed from any of these states. However, if there are con-

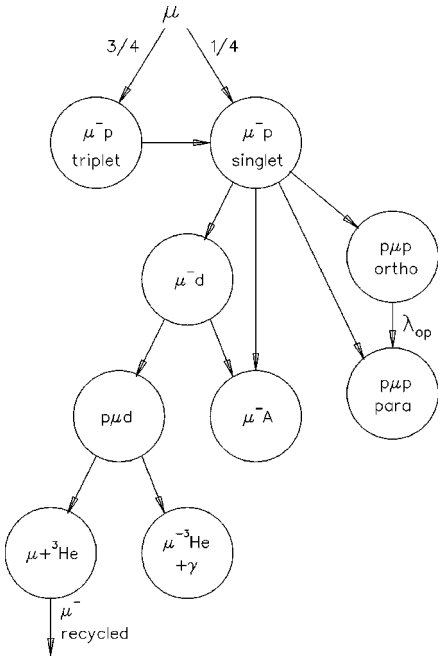

FIG. 5. Muon atomic and molecular states in liquid hydrogen.

taminants with $A>1$ the μ^- will rapidly transfer from the proton and form a μA atom. Heavy impurities ($A>2$) were reduced to $\ll 10^{-9}$ per hydrogen atom by thorough bakeout and pumping and by passing the gas through a palladium filter. If deuterium is present in the hydrogen a μd atom is formed and subsequently a $p\mu d$ molecule. The latter can form a μ^3He system via muon-induced fusion. Natural H contains >100 ppm ^{2}H and since RMC on ^{3}He is predicted to occur at about 20 times the rate on H, the background from ^{3}He would be larger than the signal. Our liquid, which contained 2 ppm ^{2}H or less, was obtained from the electrolysis of two samples of deuterium-depleted H_2O. The effect of this ^{3}He background was determined by a run with natural H (see Fig. 16).

A related background involves the possibility that the μp atom, before it decays or forms a $p\mu p$ molecule, may drift to and diffuse into the Au target wall. There it could capture after a long time and defeat the time cut described above. This background was estimated using several parameters appropriate for a liquid hydrogen target at 16 K. At this temperature the μp atom has an average velocity of

$$v=\sqrt{3kT/m_{\mu p}}=3.45\times 10^4 \text{ cm/s}. \tag{12}$$

Its mean free path $\lambda=3.6\times 10^{-8}$ cm was estimated from the number density of H_2 molecules in the liquid target. The probability that the atom drifts to the wall before disappearing is given by

$$e^{-x^2/v\lambda\tau}, \tag{13}$$

where x is the distance from the wall and $\tau=3.33\times 10^{-7}$ s is the lifetime for a μp atom to be captured into a $p\mu p$ molecule. Pessimistically assuming that muons are stopped uniformly throughout the target volume and that μp atoms drift only toward the nearest wall and not away from it, the fraction F of atoms reaching the wall is given by averaging the distance x, weighted by expression (13), over the target volume. This calculation showed that $F=4.5\times 10^{-6}$ and that μp atoms formed more than 0.7 μm from the wall do not contribute to the background. The size of this background relative to the RMC branching ratio was estimated to be

$$F\Gamma_{\text{Au}}/\Gamma_H=0.13\%, \tag{14}$$

where $\Gamma_{\text{Au}}=6\times 10^{-6}$ is the estimated branching ratio for RMC in Au for photon energies above 57 MeV, and $\Gamma_H=2.1\times 10^{-8}$ is the RMC branching ratio on hydrogen reported in this work. This estimate would be reduced by another two orders of magnitude if the actual stopping distributions and solid angle corrections were used.

Other sources of background photons were due to the finite extent and divergence of the incoming beam. Muons and pions in the muon beam might have stopped outside the hydrogen target (in the beam counters, heat shields or collimators, for example) and caused backgrounds due to muon and pion capture. Such events were effectively eliminated by geometrical cuts on the origin of the photon. The possibility that stray muons could enter the target region without first passing through the beam counters was also studied. Extensive beam tests determined the number of such muons to be negligible.

V. DATA ANALYSIS

Raw data from the cylindrical drift chamber and inner wire chamber were used to reconstruct electron and positron tracks in three dimensions. Poorly fitted tracks were rejected and the remaining electron and positron tracks were paired to form candidate photon events. Candidate events which satisfied several geometrical and kinematic conditions constituted the raw photon spectrum. TDC and ADC information from both the beam and trigger scintillators was used to remove the background photons described in the previous section. The resulting sample of RMC events was then normalized to the number of muons stopped in the liquid hydrogen target. Fits to the data with the theoretical RMC spectrum convoluted with the detector response yielded the experimental value of g_p. This section describes each of these steps in detail.

A. Event selection

The event reconstruction and selection process was designed to (1) identify e^+e^- track pairs with the correct topology for photon conversion in the Pb sheet, (2) optimize photon energy resolution to reduce the number of photons from inner and outer bremsstrahlung with reconstructed energies above 60 MeV, (3) reject photons originating from outside the target, and (4) maintain the largest possible acceptance for RMC photons. Cuts made to achieve these goals were tested by comparing their effect on real and simulated π^-p data [Eqs. (6)–(8)]. The chosen cut values left the same percentage of surviving events for real and simulated data sets. The final set of cuts was then applied identically to real μ^-, μ^+, and π^- data.

TABLE I. Conditions of acceptance for wrap-around and non-wrap-around electron and positron tracks.

Track Parameter	nonwrap e^+	wrap e^+	nonwrap e^-	wrap e^-
S_{xy}^2 (cm^2)	<0.0048	<0.027	<0.0038	<0.021
S_z^2 (cm^2)	<0.07	<2.00	<0.14	<2.00
d_{IWC} (cm)	<0.8	<0.8	<0.8	<0.8
N_{xy}	>11	>10	>11	>11
N_z	>2	>2	>2	>2
d_{apex} (cm)		>53.0		>53.0

1. Tracking cuts

Two distinct track types occurred in the spectrometer: higher momentum particles which escaped through the outer layer of the drift chamber, and lower momentum particles which spiraled around inside it. In order to maximize detector acceptance both types were kept but different values of the tracking cuts were applied to each. Both track types were subjected to cuts on S_{xy}^2 and S_z^2, the variance of the drift chamber hit coordinates from the fitted track in xy and z, respectively, the number N_{xy} of drift chamber hits per track in the xy plane, the number N_z of hits per track in z and the distance d_{IWC} of the xy projection of the drift chamber track to the nearest hit in the inner wire chamber. To the spiral, or wrap-around tracks a cut on d_{apex}, the distance from the center of the drift chamber to the most distant track point, was also applied. The cut having the largest effect on the energy resolution was S_{xy}^2. The values of these cuts for wrap-around and nonwrap-around tracks are shown in Table I.

Cut values for e^+ and e^- tracks are slightly different due to the 5.5° Lorentz angle of the drift electrons in the chamber cells. Because the curvatures of e^+ and e^- tracks are opposite, the angle between e^- tracks and the drift direction was always closer to 90° than it was for e^+ tracks. Thus there were more wire hits per drift cell and a better fit to e^- tracks. The cuts on e^- tracks were therefore generally tighter than for e^+ tracks.

2. Photon cuts

Satisfactory electron and positron tracks were paired to form photon candidates which were selected if they had conversion-pair-like topologies (see Fig. 4). For true photons the distance between the two tracks where they intersect the lead converter must be small. This distance was resolved into two components d_{xy} and d_z. The opening angle in the xy plane θ_{open} must also be small. Large opening angles and/or large converter distances were strong indications that the electron and positron tracks had been mismatched and did not represent a true photon, or that multiple scattering had distorted one or both of the tracks. A photon satisfying the above conditions could still be rejected if it did not point back to the liquid hydrogen target. Indicators of this were R_{close}, the shortest distance between the reconstructed photon momentum vector and the z axis of the target, z_{close} the longitudinal component of R_{close}, z_{rad} the z coordinate of the intersection point of the photon momentum vector with the target wall, and Δp_z, the difference of the momentum fractions $|(p_z/p_{\mathrm{tot}})_{e^+}-(p_z/p_{\mathrm{tot}})_{e^-}|$. The values of these cuts for photons which included a wrap-around track and for those that did not are shown in Table II.

TABLE II. Conditions of acceptance for photons containing a wrap-around track and photons that do not. The value of z_{cent} is the centroid of the muon stopping distribution.

Photon parameter	nonwrap	wrap
d_{xy} (cm)	<3.6	<2.5
d_z (cm)	<5.0	<5.0
R_{close} (cm)	<7.0	<9.0
$\lvert z_{\mathrm{close}}-z_{\mathrm{cent}}\rvert$ (cm)	<12.0	<12.0
$\lvert z_{\mathrm{rad}}-z_{\mathrm{cent}}\rvert$ (cm)	<16.0	<16.0
Δp_z	<0.7	<0.8
θ_{open} (°)	<31.0	<50.0

3. False photons

The charged particle rate in the cylindrical drift chamber was about 300 kHz and consisted mainly of electrons from muon decay. The A, A', and B scintillator rings vetoed these tracks with a combined inefficiency of 5×10^{-6}, making it highly unlikely that two such tracks could survive to make an accidental, or false, photon. If, however, an electron underwent hard bremsstrahlung before reaching the veto rings and the subsequent photon converted asymmetrically, the positron could have been accidentally paired with an unrelated decay electron. Other false photons could be due to (1) electrons which leaked through the veto and crossed the drift chamber in the same region as a true photon, leading to a potential mispairing of tracks, and to (2) positrons produced by photon conversion in the target paired with electrons produced by photon conversion or muon decay in the Pb converter. All such spurious tracks were removed by considering the time of a given track relative to the event time as defined by the C counters. The small coincidence window (60 ns) and the low singles rate (<40 kHz) in any individual C counter contributed to a well defined trigger time. An additional track could be removed if it occurred outside of the ±30 ns coincidence window, but within ±250 ns of the trigger time. The 250 ns interval represented the ''memory time'' of the drift chamber determined by the maximum drift time in the chamber cells. If fewer than two tracks survived this restriction, the event was discarded. Using the veto rings' efficiency it was estimated that, for the entire data sample, less than 0.1 false photon event would survive this cut in the region between 60 and 100 MeV.

B. Background subtraction

Nearly all events surviving the above cuts are true photons, the vast majority of which are due to the various backgrounds described in Sec. IV. Some of these backgrounds were identified and eliminated event by event using additional cuts, while others were estimated and subtracted using subsidiary measurements or calculations. The removal of each of these backgrounds from the raw photon spectrum is presented here, roughly in decreasing order of importance.

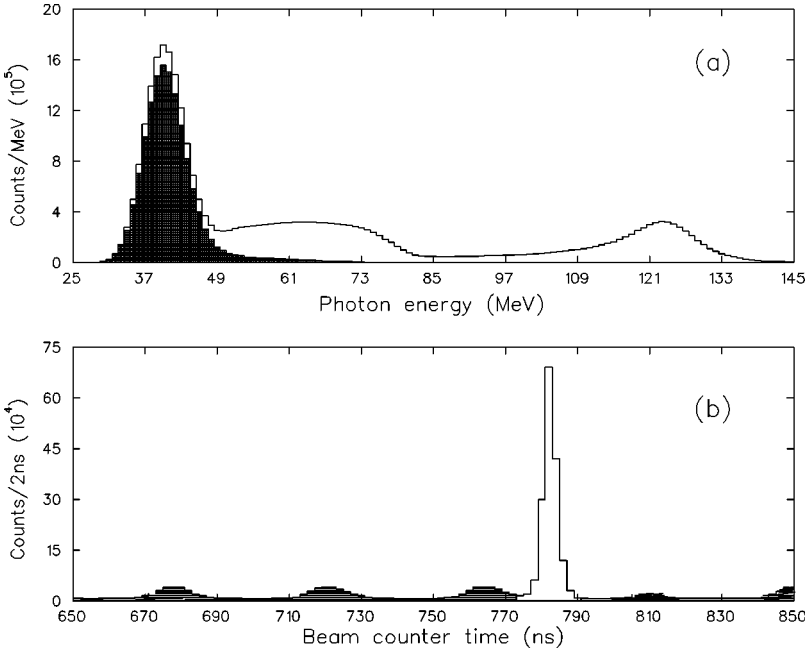

FIG. 6. (a) Raw photon spectrum with nonprompt events shaded. (b) Beam counter times within 1 μs window around trigger time with nonprompt events shaded.

1. Pion capture

As mentioned above, photons from pion capture on H [Eqs. (6)–(8)] are $\sim 10^7$ times more likely than those from RMC on H, hence the need for very efficient rejection of pion-induced events. The rf separator reduced the π/μ ratio in the beam to $R_{\rm sep}=2\times10^{-4}$ while a ''prompt'' cut removed photons due to pions which survived the separator. This cut rejected all events in which the photon trigger occurred between 60 ns before and 10 ns after the pion or muon had arrived at the beam counters. Its effect, shown in Fig. 6(a), was to remove from the photon spectrum nearly all events above 60 MeV. The remaining events were due to inner and outer bremsstrahlung, cosmic rays and RMC on Au, Ag, and H. The steep falloff below 40 MeV represents the lower limit of the detector acceptance. Figure 6(b) is a portion of a histogram of all beam counter pulse times within a 1 μs window around the trigger time and shows that the prompt events fell within a well-defined peak. The prompt cut efficiency was measured by applying it to a pion data sample of more than 10^5 events with $E_\gamma<85$ MeV. No photons survived, indicating a cut inefficiency of $<10^{-5}$. For pion-induced photons in muon data samples the prompt cut efficiency was estimated by noting that no prompt photons survived in the region $E_\gamma>100$ MeV [see Fig. 6(a)]. With 6.5×10^6 photons in this region of the raw spectrum, the cut inefficiency at 67% C.L. was $\epsilon_{\rm prompt}<1.54\times10^{-7}$.

Pions in the beam have the same momentum as muons but lose about twice as much energy in the beam counters before stopping in the hydrogen target. Therefore they stopped further upstream than the muons and a cut on the photon origin ($z_{\rm close}$ and $z_{\rm rad}$ of Table II) reduced the pion-induced photons by an additional factor of two, $R_{\rm geom}=0.5$. A conservative cut on the larger pion pulse-height in the beam counters provided another factor of 2 reduction, $R_{e\rm loss}=0.5$. The total relative reduction of pion-induced photons was thus

$$R_{\rm tot}<R_{\rm sep}\epsilon_{\rm prompt}R_{\rm geom}R_{e\rm loss}=7.7\times10^{-12}, \qquad (15)$$

indicating that this background was eliminated.

2. High-energy tail

The background component of the high-energy tail consists of photons from inner and outer bremsstrahlung [Eqs. (9)–(11)] which are reconstructed at energies above 60 MeV. The most straightforward characterization of this background is derived from a measurement of the photon spectrum generated by stopping μ^+, which contains the same bremsstrahlung events but no RMC events. However, the positron from μ^+ decay can also annihilate in flight, thereby producing a high-energy photon. The μ^+ and μ^- background spectra are therefore not identical for the same number of particles stopped in the target. Monte Carlo studies have shown that the shape of the simulated μ^+ photon spectrum is in good agreement with the experimental one (see Fig. 7), and that the ratio of μ^+-induced photons to μ^--induced photons

$$\frac{N_\gamma^{\mu^+}}{N_\gamma^{\mu^-}}=\frac{\Gamma_{\rm out}+\Gamma_{\rm in}+\Gamma_{\rm ann}}{\Gamma_{\rm out}+\Gamma_{\rm in}} \qquad (16)$$

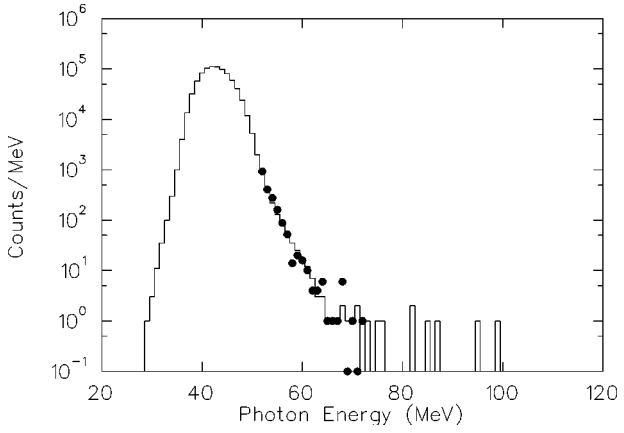

FIG. 7. μ^+ photon spectrum showing the high-energy tail (E_γ > 60 MeV). The Monte Carlo simulation of the high-energy tail is shown in black circles.

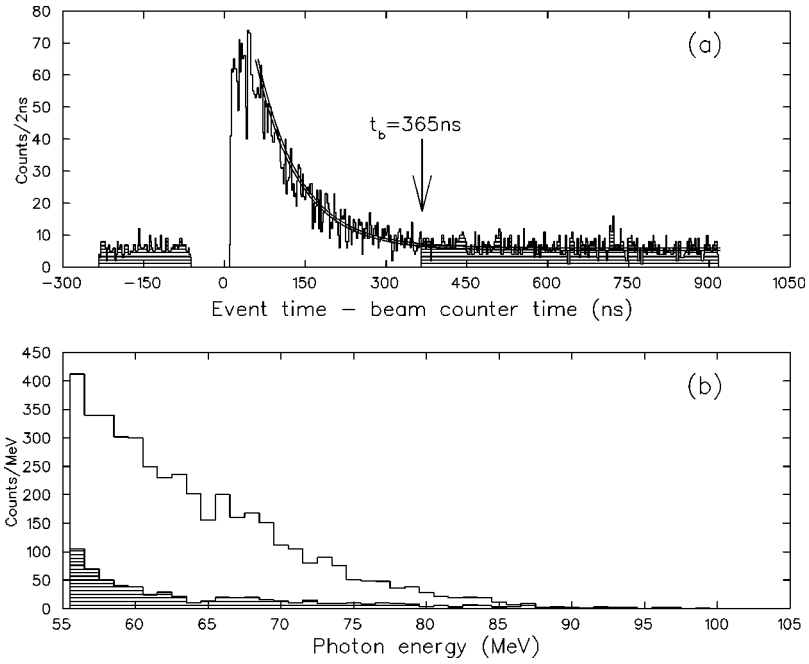

FIG. 8. (a) Photon time spectrum ($E_\gamma > 56$ MeV) showing the location of the blank time cut. The line through the histogram represents the fit to the time spectrum using the Au and Ag lifetimes. (b) The effect of the blank cut on the photon energy spectrum. In both figures the shaded regions represent events surviving the blank cut.

is, within errors, constant as a function of reconstructed energy above 52 MeV. Here Γ_{out}, Γ_{in}, and Γ_{ann} represent the probability that a stopped muon produces a photon from outer bremsstrahlung, inner bremsstrahlung, and positron annihilation, respectively. So, while the number of high-energy tail photons produced per stopped μ^+ is larger than that for μ^-, the shapes of the two spectra are the same.

This allowed the direct background subtraction from the μ^- photon spectrum using the scaled μ^+ photon spectrum. In the μ^- spectrum an energy $E = 52$ MeV was chosen, as low as possible, where the relative RMC contribution was negligible, but where the slope of the spectrum was not yet too steep. The μ^+ spectrum, shown in Fig. 7, was first corrected for cosmic-ray and beam-related background (see below) and then normalized so that the data bin at $E = 52$ MeV contained the same number of events as the corresponding bin in the μ^- spectrum. The normalized μ^+ spectrum above 60 MeV thus represented the high-energy tail corrected experimentally for positron annihilation. The number of events in the tail above 60 MeV was found to be 44 ± 7.

A second method used to obtain the high-energy tail was to generate a Monte Carlo photon spectrum containing inner and outer bremsstrahlung as well as RMC, fit this to the measured μ^- spectrum, and then subtract the RMC spectrum. The amplitude of the RMC spectrum was a free parameter in the fit but its shape was taken from theory. In this case, the number of high-energy tail events above 60 MeV was 48 ± 7, in agreement with the previous method. The high-energy tail spectrum obtained with this method is compared with the RMC spectrum in Fig. 11.

3. RMC in Ag and Au

The background from RMC on the Au target walls and the Ag collimator and heat shields was reduced by a ''blank'' cut on the time at which muons pass through the beam counters relative to the photon trigger time. Figure 8(a) shows the distribution of these times for photons with energies above 56 MeV and for which at least two beam counters fired in coincidence. The energy cutoff at 56 MeV was chosen to improve the statistics of the time spectrum which in turn allowed a better determination of the RMC background due to Au and Ag. In obtaining the final RMC spectrum ($60 < E_\gamma < 100$ MeV), only the background counts above 60 MeV were subtracted. For $10 < t < 365$ ns the shape of the spectrum is dominated by the muon lifetimes in Au and Ag, $\tau_{\text{Au}} = 73$ ns and $\tau_{\text{Ag}} = 88$ ns [36]. For $t > 365$ ns the spectrum is flat and due largely to pileup events in which the muon arrival time is uncorrelated with the trigger time. Also included in this region are events due to RMC in H which has a nearly flat distribution because of the long muon lifetime in H $\tau_H = 2195$ ns [37]. Events with $t < -60$ ns are due to pileup when the muon stops in the target after the photon trigger. The gap at $-60 < t < 10$ ns is due to the removal of the prompt events.

Keeping only events with $t > 365$ ns removed the bulk of RMC events from Au and Ag as shown in the photon spectrum in Fig. 8(b). Background events occurring at $t > 365$ ns were removed by fitting the uncut time spectrum in Fig. 8(a) with the known time behavior of muons in Au and Ag

$$\frac{dN}{dt} = A_{\text{Ag}} e^{-t/\tau_{\text{Ag}}} + A_{\text{Au}} e^{-t/\tau_{\text{Au}}} + \rho \tag{17}$$

and subtracting from the integrated photon spectrum the amount

$$N_{bkg} = P \int_{t_b}^{\infty} \left(\frac{dN}{dt} - \rho \right) dt. \tag{18}$$

Here $t_b = 365$ ns is the blanking time. ρ is the rate of time-independent background events, including pileup. It was fixed by fitting the $t < -60$ ns part of the time spectrum where there is no RMC on Au or Ag. A_{Ag}, the relative contribution of RMC on Ag, was a free parameter in the fit. A_{Au}, the contribution of RMC on Au, was then fixed by the integral under the fit. Because of the relative scarcity of

TABLE III. Background from RMC on Au and Ag for $t>365$ ns as a function of ρ.

ρ (counts/2 ns)	A_{Ag} (counts/2 ns)	A_{Au} (counts/2 ns)	N_{bkg}
5.0	94 ± 15	29 ± 20	56 ± 5
5.6	51 ± 15	76 ± 20	41 ± 5
6.2	7 ± 15	125 ± 20	26 ± 5

RMC on H events, no term for the muon lifetime in H was included in the fit. A maximum likelihood fit of the flat region of the time spectrum ($t<-60$ ns) yielded $\rho=5.6\pm0.6$ counts/2 ns with most of the error due to statistics. Fits of the uncut time spectrum for $\rho=5.0$, 5.6, and 6.2 gave values for A_{Au}, A_{Ag}, and hence N_{bkg} which are shown in Table III. Since the error in ρ dominated the evaluation of N_{bkg}, the error in N_{bkg} was enlarged to include the extreme values determined for $\rho=5.0$ and $\rho=6.2$. Thus, for $E_\gamma>56$ MeV, $N_{bkg}=41\pm15$. Under the RMC signal region $60<E_\gamma<100$ MeV, $N_{bkg}=29\pm11$.

The factor P is introduced by the effective dead time of 365 ns after the trigger time. It is the probability that a second beam muon does not arrive within the blanking time and veto the event. Ideally P is given by Poisson statistics

$$P=e^{-r\Delta t}=0.786, \tag{19}$$

where $\Delta t=365$ ns and $r=658$ kHz, the incident muon rate averaged over all running periods. P was measured for each running period by finding the ratio R of the number of events after to those before the blank cut. R is given by the probability that a muon decays after the blanking time, times P. In principle, P can be extracted using

$$R=Pe^{-365/\tau_H}=0.847P \tag{20}$$

or

$$P=1.18R. \tag{21}$$

However, due to such effects as dead time in the beam counters, beam microstructure, the prompt cut and the fact that not all muons passing through the beam counters stop and decay in the target, corrections to Eq. (21) are required. These were performed in a Monte Carlo simulation of muon arrival times as a function of incident muon rate. The result is that Eq. (21) is modified, and can be rewritten as

$$P=1.39R-0.19. \tag{22}$$

The value of R, averaged over all data runs, was 0.676 ± 0.008. Substituting into Eq. (22) yielded $P=0.75\pm0.011$, only 5% smaller than expected from Eq. (19).

4. Cosmic rays and beam-related radiation

The intensity at sea level of cosmic ray muons above 1 GeV/c is 70 m^{-2} s^{-1} sterad^{-1} [38]. These can cause background photons from electromagnetic showers when they enter the detector. Photons induced by muons or other charged particles were, in part, removed through the use of the cosmic ray active veto described earlier. Hence cosmic ray neutrons were found to be a greater background since they undergo hadronic production of π^0's in the iron of the detector magnet. With the cyclotron off the photon trigger rate in the detector was roughly 0.1 s^{-1}, clearly non-negligible compared to the rate of RMC in hydrogen. With the cyclotron on, ambient activity, mainly from production target neutrons, was another background source.

The bulk of cosmic-ray-induced photons were removed in software by noting that they were usually accompanied by charged particle tracks. Photons were removed if a charged particle track in the same event fired a cosmic ray drift chamber and the cosmic ray scintillator directly beneath it. Candidate e^+e^- pairs were also rejected if the C or D counter opposite the pair fired.

When high-energy neutrons from cosmic rays or the M9A production target produce π^0's, the resulting photons might not be accompanied by charged particles and therefore they cannot be directly vetoed. Since the source of these photons is not localized, cuts on their direction and origin will distinguish them from RMC photons which originate at the center of the liquid hydrogen target. However this would not remove all background events. To do so, background data runs were taken under beam-off and beam-on conditions and analyzed using the same cuts as for nonbackground runs. During beam-off runs the cyclotron was off, so only cosmic ray background could be present. During beam-on runs there was current in other beamlines but not in M9A, so that the sum of cosmic and beam-related backgrounds was sampled. The two components were then separated using the relation

$$N_{bkg}=R_{\mathrm{cosmic}}t_{\mathrm{live}}+R_{\mathrm{beam}}Q, \tag{23}$$

where t_{live} is the live time or total time in days that the experiment was accepting triggers. Q is a measurement of the total charge striking the production target in the main beamline during the run, and is corrected for experiment dead time. Its units are arbitrary but proportional to μA h. Q was also assumed to be proportional to the ambient flux of beam-related activity through the detector. The rate of cosmic-ray-related photons R_{cosmic} and the rate of beam-related photons R_{beam} were determined by sampling background photons in the range $0<E_\gamma<200$ MeV over a four-year period. After cuts there were 60 beam-off events over a period of 92 days with $Q=0$, so that R_{cosmic} was found to be 0.65 ± 0.08 events per day. Under beam-on conditions there were 111 events over a period of 102 days with $Q=8703$. Solving for R_{beam} yielded 0.0051 ± 0.0015 events per unit charge Q or 0.44 beam-related events per day for the typical beam currents during the experiment.

Over the entire period of RMC data taking, the experiment was live for 66.85 days and collected a total charge $Q=6326$. The number of background photons expected in the RMC data was therefore

$$N_{bkg}=(R_{\mathrm{cosmic}}t_{\mathrm{live}}+R_{\mathrm{beam}}Q)P \tag{24}$$

$$=[0.65\times66.85+0.0051\times6326]0.75$$

$$=57\pm8, \tag{25}$$

where $P=0.75$ is the blank-pile-up correction described earlier. Assuming that the shape of the cosmic and beam-related

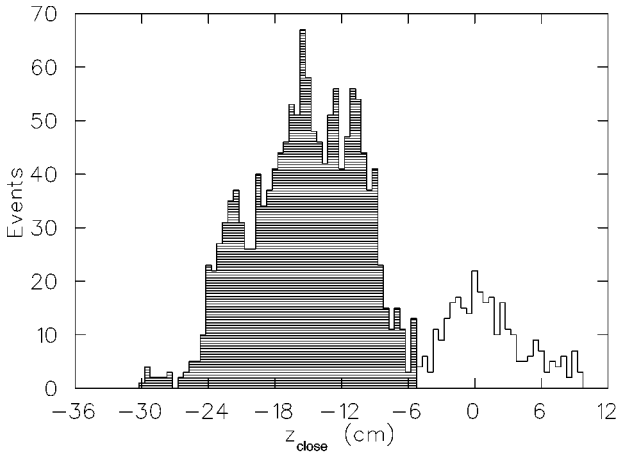

FIG. 9. Distribution of z_{close}, the z component of the point of closest approach of the photon momentum vector to the z axis. The shaded region represents those events which are removed by a cut on R_{close}.

background was the same for the RMC data runs and the beam-on background runs, 29 ± 9 of these photons fell in the RMC signal region, $60<E_\gamma<100$ MeV, and had to be subtracted. 23 ± 7 events were expected to occur in the region $100<E_\gamma<200$ MeV. The error bars on these numbers reflect, in part, the uncertainty in the shape of the background spectrum. As a check on this subtraction, events in the RMC spectrum between 100 and 200 MeV, where no RMC events should occur, were analyzed. After the same cuts were placed on these events as on those below 100 MeV, 24 ± 5 events remained, in agreement with the 23 background events expected in that region.

The above procedure was repeated for μ^+ data so that the subtraction of the high-energy tail could be done correctly. In this case the beam-on background run was the same except that the polarity of the M9A channel magnets was now positive. Based on the measured rates for 14.85 days of livetime, the number of beam-on background photons in the μ^+ spectrum was predicted to be 14 ± 6 between 0 and 200 MeV. Of these, 6 ± 2 were between 60 and 100 MeV and 5 ± 2 were between 100 and 200 MeV. The observed value of 7 ± 3 events between 100 and 200 MeV is in agreement with prediction.

5. Stops outside the LH_2 target

Monte Carlo beam transport calculations estimated that 35% of the incident muon beam stopped in the Pb collimator which is located immediately upstream of the beam counters (see Fig. 2). These muons, and contamination pions, could then produce photons through RMC or radiative pion capture (RPC) in Pb. The photon would likely pass through the beam counters without firing them, thus adding a photon background flat in time and very similar to RMC in H. Since these photons originated well upstream of the normal muon stopping location the cuts on the photon origin, z_{rad} and z_{close} removed most such events. This is demonstrated by the distribution of z_{close} shown in Fig. 9. As described in Sec. V A, z_{close} is the longitudinal component of the vector R_{close}, which is the point of closest approach of the reconstructed photon momentum vector to the z axis. Photons with $z_{close}<-5$ cm were removed by a cut on R_{close}. Photons with $z_{close}>-5$ cm were centered on $z=0$ as expected for RMC events from the hydrogen target. Due to imperfect position and momentum resolution, some photons originating upstream of -5 cm may have been reconstructed as photons originating inside the target, thereby introducing a background from stops outside the target. The estimated number of such events was 9 ± 5.

The few pions in the muon beam which were not rejected by pulse height and timing in the beam counters could have decayed in flight to produce muons which stopped and captured in the Au/Cu backplate of the hydrogen target. The beam simulation which reproduced the observed stopping distribution in the target indicated that the number of such events was small and cuts on the photon origin reduced them to a negligible level. Similarly the RMC background from uncounted muons stopping in the target backplate was found to be negligible due to the same restrictions on photon origin.

It was also possible that a few stray muons from the fringes of the beam passed through the vent holes upstream of the beam counters without passing through the beam counters (see Fig. 2). If they subsequently stopped in the A or A' ring of veto scintillators immediately outside of the target or in the target's Ag vacuum jacket or heat shield, and then underwent RMC, the resulting photons would appear to have a flat time spectrum, mimicking RMC on H. Monte Carlo beam studies estimated that a 1% RMC background from Ag and C would occur if 10^{-4} of all muons got to the Ag and veto counters without being counted. In order to look for uncounted muons, beam tests were performed in which a scintillator replaced the hydrogen target. The beam counters were placed in anti-coincidence with the scintillator so that only muons not passing through the beam counters would be collected. Over several beam test periods no such events were found, setting an upper limit on uncounted muons of $<1.6\times10^{-5}$ at 67% C.L. This indicated that the total background from this source was less than 0.2% of the RMC signal.

6. Target impurities

In impure liquid hydrogen the rate at which muons dissociate from μp atoms to form μA atoms is of the order 10^{11} s^{-1} which greatly enhances the probability of RMC on heavy ($A>2$) impurities in the target. Impurity levels of $\simeq10^{-9}$ per hydrogen atom were therefore required. Repeated bakeout of the target vessel and a special hydrogen gas storage and purification system [33] were used to achieve the necessary purity. Since gas impurities of 10^{-9} per atom are not measurable using mass spectrometers, an indirect test was performed. The pressure change at the output valve of the palladium purifier was measured with an ion gauge as likely target contaminants such as N, Ar, and Ne were admitted at the input valve. The very small pressure change indicated that the target contamination could be no more than 1 atom in 10^{13}. In the unlikely event that impurities did enter the target, they would have frozen to the target walls at the operating temperature of 16 K.

The palladium purifier will, however, pass deuterium. For this reason deuterium-depleted water [39] was electrolyzed to obtain isotopically pure hydrogen gas which was later purified of heavy gases and liquified in the target vessel.

Throughout the course of the experiment gas samples were extracted directly from the target and the deuterium level was measured using a mass spectrometer [40]. For the two sources of water used during the experiment, the deuterium levels were 2 ppm and <0.1 ppm (below the 0.2 ppm sensitivity of the mass spectrometer). The weighted average for these samples was 0.6 ± 0.1 ppm. This deuterium concentration was low enough to guarantee that the photon background from the chain $\mu p\rightarrow\mu d\rightarrow\mu^3He\rightarrow$RMC on ^{3}He was small relative to RMC in hydrogen. While this chain is expected to be dominant, other deuterium-related branches may contribute. To measure and subtract all deuterium-related backgrounds another RMC data sample was taken using liquid hydrogen with natural deuterium abundance, in this case 117 ppm. The number of photons from RMC on ^{3}He could then be found by extrapolation to zero deuterium concentration. Using the measured rates [41–49] for the transitions between μ-atomic and μ-molecular species shown in Fig. 5, the ratio

$$R_d=\frac{\Gamma_{0.6}-\Gamma_0}{\Gamma_{117}-\Gamma_{0.6}}=(0.77\pm0.11)\times10^{-2} \tag{26}$$

was calculated. Here Γ_0 is the theoretically predicted branching ratio for RMC in ^{1}H and $\Gamma_{0.6}$ and Γ_{117} are the total theoretical branching ratios for RMC in all atomic and molecular species for deuterium concentrations of 0.6 and 117 ppm, respectively. Because the muon transfer rate from μp to μd (1.0×10^{10} s^{-1}) is large compared to that from μp to $p\mu p$ (2.5×10^6 s^{-1}), which in turn is large compared to the many other transfer and reaction rates involved, the branching ratios Γ are nearly linearly dependent on the deuterium concentration. The ratio R_d effectively removes all dependence on the other parameters, including the expected RMC rates in ^{1}H (0.03 s^{-1}) and ^{3}He (0.676 s^{-1}) [50]. Variation of the RMC rates over wide ranges and of the transfer rates over their measured uncertainties yielded the value and total uncertainty in R_d given in Eq. (26). Experimental values of $\Gamma_{0.6}$ and Γ_{117} were used along with R_d to calculate the ^{3}He background

$$\Gamma_{0.6}-\Gamma_0=R_d(\Gamma_{117}-\Gamma_{0.6}). \tag{27}$$

For $E_\gamma>60$ MeV this was 3 ± 1 events.

7. Other backgrounds

About 0.1% of negative muons entering the liquid hydrogen target and becoming bound in atomic orbitals undergo capture on the proton. The rest decay while bound, producing a decay electron which may have energies up to m_μ and which may undergo bremsstrahlung causing a potential background for RMC. However, it has been shown [51,52] that the electron spectrum falls rapidly above $E_e=m_\mu/2$, so that the rate for this process above 58 MeV is 15 times less than the rate for RMC on H. In addition, the rate of such events would be suppressed by a factor of order 10^4 because the photon would be accompanied by a charged particle track from the target. The spectrum for bound radiative muon decay has not been calculated but should be reduced by a factor α from the nonradiative case and therefore will also be a negligible background.

TABLE IV. Summary of subtracted backgrounds.

Source	Counts
Total photons after cuts ($60<E_\gamma<100$ MeV)	397 ± 20
High-energy tail	48 ± 7
Cosmic ray+beam related	29 ± 9
RMC in Au and Ag	29 ± 11
π, μ stops away from target	9 ± 5
RMC in ^{3}He	3 ± 1
RMC in ^{1}H	279 ± 26

In the 63 MeV/c incident muon beam, the electron contamination is about 5%. Some of these electrons may undergo hard bremsstrahlung, producing photons up to 62 MeV. Such events are very efficiently suppressed by cuts on low pulse height and prompt timing in the beam counters. The electron-induced events which survive are further suppressed by a factor 10^4 by the charged-particle veto counters. This background is therefore negligible. The backgrounds subtracted from the after-cuts RMC spectrum are summarized in Table IV.

C. Normalization

The number of photons detected after cuts and background subtraction can be written analytically as

$$N_\gamma=N_{\rm stops}K\int dk'\int dk\frac{d\Gamma}{dk}(k)A(k',k), \tag{28}$$

where $N_{\rm stops}$ is the number of muons stopping in the target and K is the product of various corrections and efficiencies (see Sec. V D). $A(k',k)$ is the measured detector response to a photon of energy k, and k' is the reconstructed photon energy. $d\Gamma/dk$ is the RMC branching ratio, the integral of which can be extracted once N_γ has been measured.

The number of stops in the liquid hydrogen target could not be measured directly but had to be related to the measured flux of muons through the beam counter scintillators located 17 cm upstream of the center of the target. For a muon to be counted it had to pass through all four beam scintillators in time with the cyclotron rf and in anticoincidence with the master veto from the data acquisition system. The sum $N_{\rm beam\ rf\ \overline{MV}}$ was then corrected for each data run by several factors to get the true number of stops in the target:

$$N_{\rm stops}=N_{\rm beam\ rf\ \overline{MV}}f_{bm}\eta_o\eta_u\eta_m/\epsilon_{bm}. \tag{29}$$

f_{bm} is the fraction of muons passing through all four beam counters which also stop in the target. Due to several effects such as beam divergence, multiple scattering and muon decay, $f_{bm}<1$. It was measured in a test run in which the liquid hydrogen target was replaced by a copper-walled mock-up target of the same size and shape. A plastic scintillation counter was fitted tightly inside the target and its signal was taken in coincidence with the four beam counters and the cyclotron rf signal. f_{bm} was then given by

$$f_{bm\mu}=N_{\rm beam\ rf\ \overline{MV}\,TGT}/N_{\rm beam\ rf\ \overline{MV}}=0.926\pm0.005. \tag{30}$$

This measured value was found to agree (to within 1%) with a REVMOC [53] Monte Carlo simulation of the beam and target arrangement. The same exercise was performed for 81 MeV/c pions with the result

$$f_{bm\pi}=0.85\pm0.01, \tag{31}$$

also in 1% agreement with the Monte Carlo simulation. $f_{bm\pi}$ is smaller than $f_{bm\mu}$ due to pion decay in flight and to the fact that the incident pion momentum is higher than the incident muon momentum.

η_o is a correction for the overcounting of muon stops. Some electrons from muon decay in and around the target may have passed through and fired all four beam counters, thus registering spurious muon counts. The beam counters subtend an average solid angle of 0.0318 from the point of muon decay, assuming isotropic decay, and the probability that an effectively random decay electron coincides with the rf time is 0.58. η_o is therefore $1-0.0318(0.58)=0.980\pm0.007$ and is independent of beam rate. η_u corrects for the undercounting of stops due to the location of the rf timing window used to reject pions and electrons in the beam. Moving the window to efficiently reject beam electrons meant that some muons may miss the coincidence and not be counted. The size of this effect was estimated using prescaled beam-sample events which record beam counter and trigger information in the absence of a photon trigger. The fraction of muons missed is given by the number of beam counter pulses whose heights are consistent with muon energy loss and which are out of coincidence with the rf window. That fraction was found to be 1.6% leading to $\eta_u=1.016\pm0.009$. This correction is also independent of the beam rate.

A further correction was required to account for multiple muons per beam burst and the microstructure of the beam. η_m is rate dependent and is given by Poisson statistics:

$$\eta_m=\frac{r\Delta t}{1-e^{-r\Delta t}}=1.014, \tag{32}$$

where $r=658$ kHz is the average beam rate and $\Delta t=43.3$ ns is the time between beam bursts. For pion calibration runs the beam rate was lower and the effect smaller with $\eta_m=1.005$. Finally, ϵ_{bm} is the combined efficiency of the four beam counters for muons and is 0.984 ± 0.003. For pions it is 1.00. ϵ_{bm} is the product of the individual beam counter efficiencies, each measured by taking the ratio of the appropriate threefold coincidences to the fourfold coincidences. Using Eq. (29), the number of true stops in the target for all data runs is

$$N_{\text{stops}}=(3.46\pm0.05)\times10^{12}, \tag{33}$$

where the number of muons counted by the beam scintillators $N_{\text{beam rf }\overline{MV}}$ over all data runs was 3.637×10^{12}.

D. Detector response

Over the course of the experiment the beam was periodically tuned for 81 MeV/c π^-, which stopped in the target at the same place as the 63 MeV/c μ^-. The resulting pion-induced photons were subjected to the same geometrical cuts as the muon-induced photons, but not to timing cuts. The resulting spectrum was used to obtain the response function $A(k',k)$ of the spectrometer to the well known photon spectrum from pion capture [Eqs. (6)–(8)]. This was done with a GEANT [54] Monte Carlo simulation which reproduced the shape and absolute magnitude of the experimental π^-p spectrum. It was then assumed that the response function determined for pion-induced photons was the same as that for muon-induced photons. Included in the Monte Carlo simulation was a careful reproduction of the entire spectrometer geometry and mass distribution, a detailed treatment of electron drift characteristics in each cell of the drift chamber, muon and pion beam parametrizations verified by beam tests and all relevant physical processes down to 1 MeV for photons and electrons and 100 keV for muons. Not included were the C-counter efficiencies, various corrections due to cuts, muon pileup, electronic noise and changes in acceptance over time, all of which comprise the factor K of Eq. (28). The effects not included, discussed below, were measured directly and then applied to the Monte Carlo generated spectra to get the final response function.

1. Response function

The response function includes the geometrical acceptance of photons in the spectrometer, the probability that photons from the target are converted into e^+e^- pairs and the energy resolution line shape. It is determined by generating Monte Carlo photons sampled from the known π^-p spectrum of Eqs. (6)–(8), whose origins in the target are identical with the pion stopping distribution. Normalizing by the number of pions stopping in the target and applying efficiencies and cut corrections analogous to the factor K in Eq. (28) yields the photon spectrum

$$N_\gamma(k')=N_{\pi\text{stops}}K_\pi\int dk\frac{d\Gamma_\pi}{dk}A(k',k). \tag{34}$$

Here $d\Gamma_\pi/dk$ is the known differential π^-p photon spectrum and $N_{\pi\text{stops}}$ is calculated in the same way as N_{stops} of Eq. (29), but with corrections and efficiencies measured for pions. If the efficiencies, corrections and number of stops are measured correctly, $N_\gamma(k')$ will be identical to the measured π^-p spectrum. Figure 10 compares the Monte Carlo spectrum with that obtained in a particular π^-p calibration run. Agreement between the two is excellent, especially in the RMC signal region of 60–100 MeV. The energy scale of the spectrometer is determined by the response to both monoenergetic photons from $\pi^-p\rightarrow\gamma n$ and the sharp upper edge of the photon distribution from $\pi^-p\rightarrow\pi^0n$, $\pi^0\rightarrow\gamma\gamma$. The uncertainty in the measured energy scale, which was found to be 0.25 MeV, introduces a 2% error in the measured RMC rate (or ±6 events).

During the course of the experiment the shape of the spectrum remained constant but the overall normalization did not. Due to variations in amplifier noise, trigger counter efficiency and event reconstruction efficiency, this factor varied by as much as 10% over a four year period, but never more than a few percent over any one running period. In all cases the RMC spectrum for each running period was corrected for the change in acceptance measured in the π^-p calibration runs. For all data taking periods the average acceptance, rela-

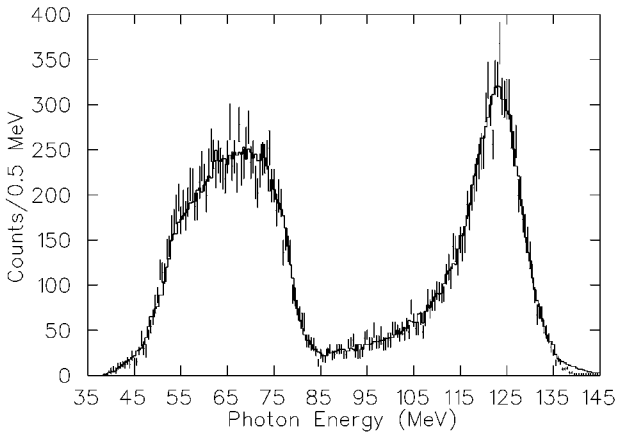

FIG. 10. The Monte Carlo spectrometer response (histogram) compared to data (bars) for photons from $\pi^- p$ reactions [Eqs. (6)–(8)].

tive to Monte Carlo, was found to be $A_r = 0.960 \pm 0.016$. Using this same photon spectrometer, a measurement of RMC on Ca [25] obtained excellent agreement with earlier measurements, indicating that the detector's response function was well understood.

2. Cut corrections and efficiencies

Cuts applied to the RMC data sample to remove background events also removed a small number of valid events. The background-free Monte Carlo data must then be corrected for the removal of good events.

The correction $\epsilon_{\cos}$ is the efficiency of the cut used to remove cosmic-ray-induced photon events. As discussed in Sec. V B, this cut was applied only to events in which no accompanying charged particle was recorded in the cosmic ray veto detectors. $\epsilon_{\cos}$ was measured using pion-induced prompt photons with energies between 100 and 140 MeV. These photons are above the RMC energy region and arise from pions in the muon beam which produce monoenergetic photons through $\pi^- p \rightarrow \gamma n$. The fraction $\epsilon_{\cos}$ of photons between 100 and 140 MeV which survived the cosmic cut was found to be 0.92 ± 0.01. Because the cosmic cut removed valid events largely due to accidental coincidences, it was assumed that the value of $\epsilon_{\cos}$ was energy independent and applied as well to photons in the RMC signal region of 60 to 100 MeV.

The fraction $1 - \epsilon_v$ gives the probability that a valid event was vetoed by uncorrelated charged particles (usually from normal μ decay) striking the A, A', or B scintillator rings. An event was vetoed if it was in time (within 60 ns) with the firing of one or more of the above scintillator rings. ϵ_v, which depends linearly on the stopping rate, was measured by determining the number of events in which a scintillator ring fired more than 150 ns before or after the event time. This was far enough from the coincidence window to ensure that the time spectrum of the charged particles was flat. Averaged over all runs, ϵ_v was found to be 0.975 ± 0.005.

A cut which removes false photons was discussed in Sec. V A. The correction due to this cut ϵ_f was measured using prompt photons with energies between 50 and 85 MeV, overlapping the RMC energy range. These photons arose from pions in the muon beam which underwent charge exchange in the target [Eqs. (6),(7)]. The fraction of such photons surviving the cut was $\epsilon_f = 0.979 \pm 0.005$.

A small number of events taken during μ^- running exhibited prompt timing with respect to the beam counters and yet were not removed by the prompt cut because only a single beam counter fired. These may have been due to beam electrons undergoing hard bremsstrahlung and producing detectable photons or to radiative muon decays in which the decay electron struck one of the beam counters. A single-hit prompt cut was added to the normal multihit prompt cut in order to reject these events. The correction to be applied to Monte Carlo data was measured by applying the modified prompt cut to the coincidence time spectrum in a region where only random coincidences occurred. The probability ϵ_s that a valid event survived this cut was found to be 0.997 ± 0.006.

The correction factor P was discussed in Sec. V B. Its value is 0.750 ± 0.011.

The trigger efficiency of the spectrometer is given by the product of the C-ring counter efficiency and the D-ring counter efficiency since one or more C counters and one or more D counters had to fire to trigger an event. The measured D counter efficiencies were incorporated into the Monte Carlo simulation while the C counter efficiencies were not. The probability ϵ_{cc} that a C counter was fired by a converted photon was measured by collecting two-photon events from π^0 decays from $\pi^- p \rightarrow \pi^0 n$. Two spatially separated, converted photons were required—one to trigger the event and the other to measure the C counter efficiency. The standard photon trigger, described earlier, was modified to bias in favor of such events by requiring that four or more D counters fired in conjunction with one or more C counters. ϵ_{cc} was then taken to be the ratio of the number of events in which two nonadjacent C counters fired to the number of events in which the same two C counters should have fired based on the reconstructed photon conversion points. For all twelve counters in the ring ϵ_{cc} was found to be 0.975 ± 0.002.

Combining the above efficiencies yields

$$\epsilon_{\text{tot}} = \epsilon_{cc} \epsilon_f \epsilon_{\cos} \epsilon_s \epsilon_v = 0.854 \pm 0.012. \tag{35}$$

Including the corrections due to pileup and relative acceptance yields

$$K = \epsilon_{\text{tot}} P A_r = 0.615 \pm 0.016. \tag{36}$$

E. Extraction of RMC branching ratio and g_p

The RMC spectrum after all cuts have been applied but before any backgrounds have been subtracted is shown in Fig. 11. Also shown is the spectrum of the high-energy tail, mainly due to bremsstrahlung (see Sec. V B), which is the largest single background to be subtracted.

The net RMC spectrum after all cuts and background subtraction is shown in Fig. 12 and contains $N_{\text{signal}} = 279 \pm 26$ RMC events above 60 MeV. In order to extract g_p and the partial RMC branching ratio from this spectrum the calculation of Fearing and Beder [29] was used. Taking the ratio g_p/g_a and the ortho to para $p\mu p$ transition rate λ_{op} as inputs, the Fearing-Beder code generated the differential branching ratio $d\Gamma/dk$. The product of the integrated branch-

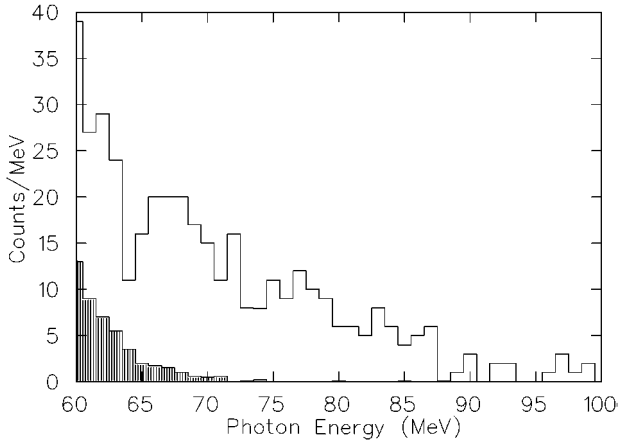

FIG. 11. Photon energy spectrum after all cuts but before background subtraction (unshaded) and bremsstrahlung background spectrum (shaded).

ing ratio, the measured number of stopped muons and the measured correction factors discussed in the previous section gives the number of RMC photons produced in the target

$$N_{\mathrm{RMC}}=R_{\gamma}N_{\mathrm{stops}}K. \tag{37}$$

The number of RMC photons detected is given by

$$N_{\mathrm{signal}}=R_{\gamma}N_{\mathrm{stops}}KA_{a}, \tag{38}$$

where A_a is the absolute spectrometer acceptance for photons. The branching ratio

$$R_{\gamma}=\int dk\frac{d\Gamma}{dk}=\int_{60}^{k_{\max}}dk\int_{365}^{\infty}dt\frac{d^2\Gamma}{dkdt} \tag{39}$$

is the ratio of the number of photons produced above 60 MeV and after 365 ns, to the number of muons present after 365 ns. Here $k_{\max}$ is the endpoint photon energy $\sim$100 MeV. R_{γ} includes the contributions to RMC from the μp singlet atomic state and the $p\mu p$ ortho- and para-molecular states

$$R_{\gamma}=f_s\Gamma_s+f_o\Gamma_o+f_p\Gamma_p. \tag{40}$$

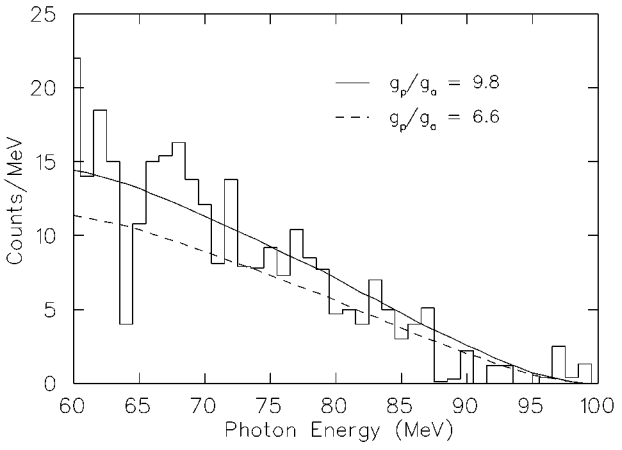

FIG. 12. Photon energy spectrum after all cuts and background subtraction. Theoretical RMC spectra are shown for the best fit value of $g_p/g_a=9.8$ (solid curve) and for $g_p/g_a=6.6$ (dashed curve).

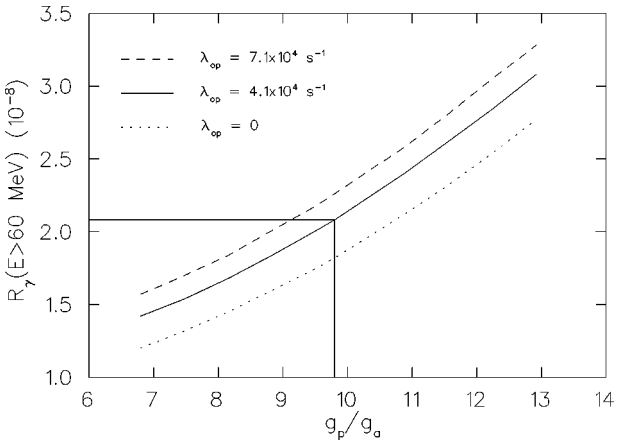

FIG. 13. Integrated RMC branching ratio ($t>365$ ns, $E_{\gamma}>60$ MeV) as a function of g_p/g_a for three values of the ortho to para transition rate λ_{op}. The solid line box indicates the value $g_p/g_a=9.8$ which corresponds to the branching ratio $R_{\gamma}=2.10\times10^{-8}$ for $\lambda_{op}=4.1\times10^{4}\ \mathrm{s}^{-1}$.

Here Γ_s, Γ_o, and Γ_p are the time-independent branching ratios for $k>60$ MeV for the singlet, ortho, and para states, and $f_s=0.061$, $f_o=0.854$, and $f_p=0.085$ are the relative occupancies of the muon in these three states. These occupancies were calculated using the measured transfer rates [41–49] between μ-atomic and μ-molecular species shown in Fig. 5, and integrating over all times longer than 365 ns. While the sum of the relative occupancies is constrained to one, their individual values depend mainly on λ_{op}. Thus the value of g_p deduced from the measured R_{γ} also depends on λ_{op}.

The Monte Carlo simulation generated 10^7 photons sampled from the calculated spectrum shape and propagated them through the spectrometer. The surviving sample of Monte Carlo events, reconstructed with the same routines used for actual data, was then normalized by a factor $N_{\mathrm{RMC}}/10^7$ and compared to the measured spectrum of Fig. 12. The value of g_p/g_a was then changed and the above process repeated until the best fit with the data above 60 MeV was attained. The curve and corresponding value $g_p/g_a=9.8$ which gave the best fit is also shown in Fig. 12. The shape of the spectrum is well reproduced by the theoretical curve, indicating that the q^2 dependence is reasonably well understood. The dependence of $R_{\gamma}(k>60)$ on g_p/g_a is shown in Fig. 13 for three values of λ_{op}.

For $g_p/g_a=9.8$ and the experimental value of $\lambda_{op}=4.1\times10^{4}\ \mathrm{s}^{-1}$ the partial RMC branching ratio is

$$R_{\gamma}(k>60\ \ \mathrm{MeV})=(2.10\pm0.21)\times10^{-8}. \tag{41}$$

The error in $R_{\gamma}(k>60)$ was obtained by solving Eq. (38) for R_{γ}, taking A_a to be its Monte Carlo value and propagating the combined statistical and systematic errors from N_{stops}, K, and N_{signal}. These errors are summarized in Table V.

Referring to Fig. 13, an error of $\pm0.21\times10^{-8}$ in the partial branching ratio yielded an error of ±0.7 in g_p/g_a. For $R_{\gamma}(k>60)$ constant at 2.10×10^{-8}, the 30% error in λ_{op} led to a separate systematic error in g_p/g_a of ±0.3. Hence

$$g_p/g_a=9.8\pm0.7\pm0.3. \tag{42}$$

TABLE V. Summary of contributions to the error in R_γ.

Source of error	% error
Net RMC events N_{signal}	9.3
Relative acceptance A_r	1.7
Blank-time correction P	1.5
Efficiencies and corrections ϵ_{tot}	1.4
Number of μ stops N_{stops}	1.4
Total percentage error in R_γ	9.8

In general g_p is influenced not just by λ_{op} but by other muon transfer and capture rates, a summary of which is given in [1]. However, variations of each of these rates over their experimental error bars produced negligible effects. For example, the value of the $p\mu p$ formation rate used in the present analysis was $\lambda_{p\mu p}=2.5\times10^6\ \text{s}^{-1}$, an average of experimental values [41–44]. Using the most recent measurement, $\lambda_{p\mu p}=3.21\times10^6\ \text{s}^{-1}$ [55], resulted in only a 2.3% increase in the RMC rate.

The extracted values of g_p/g_a and R_γ are independent of variations in the low-energy photon cutoff and the blanking time used in the analysis. Figure 14 shows that g_p/g_a does not vary with values of the low-energy cutoff greater than 60 MeV, indicating that backgrounds due to the high-energy tail of bremsstrahlung and radiative muon decay have been properly removed. Figure 15 shows that g_p/g_a is also independent of the blanking time t_b. Figure 16 shows that the number of RMC events per muon stop, and therefore g_p/g_a, is constant within statistics over all running periods. The data point for run period 3 was taken using a hydrogen target with natural deuterium abundance. It was used as a calibration of the deuterium contamination in the target and was not included in the final hydrogen RMC data sample.

VI. RESULTS AND CONCLUSIONS

The relevant energy and time windows for our experimental results are $k>60$ MeV and $t>365$ ns, where k is the detected photon energy and t is the time of detection relative to the time of the last muon stop. In this time window and for the experimental value of λ_{op} the probabilities that the muon

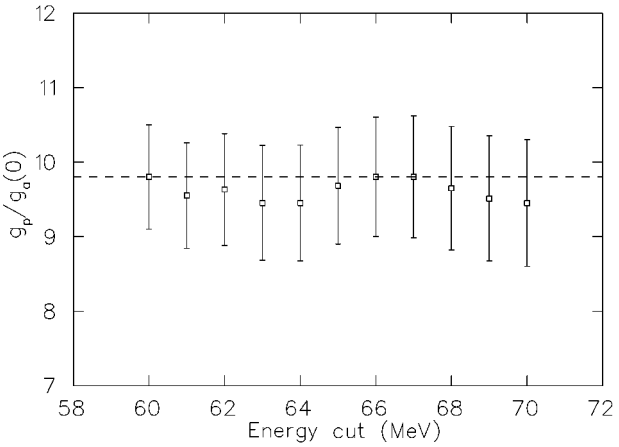

FIG. 14. g_p/g_a as a function of low-energy photon cutoff. For reference the dashed line indicates $g_p/g_a=9.8$.

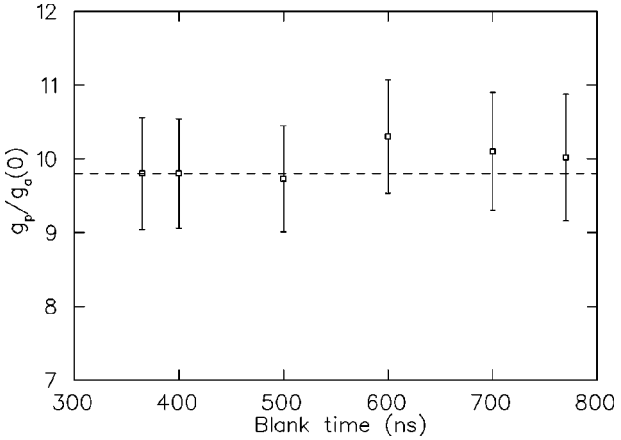

FIG. 15. g_p/g_a as a function of blanking time for $E_\gamma>60$ MeV. For reference the dashed line indicates $g_p/g_a=9.8$.

is in the μp singlet atomic state, the $p\mu p$ para molecular state, and the $p\mu p$ ortho molecular state are 0.061, 0.085, and 0.854, respectively, at the time of muon capture. These probabilities allow a comparison of any new calculation of the partial branching ratio R_γ, which for photons in our energy window was measured to be $(2.10\pm0.21)\times10^{-8}$.

The extraction of the pseudoscalar coupling g_p from R_γ is based on the latest calculation [29] of the branching ratio using g_p as a parameter. Both R_γ and dR_γ/dk were evaluated in terms of g_p with a q^2 dependence given by

$$g_p(q^2)=A_{gp}g_a(0)\frac{m_\pi^2+0.88m_\mu^2}{m_\pi^2-q^2} \tag{43}$$

for each of the contributing muonic states. The value of $A_{gp}=g_p(q^2=-0.88m_\mu^2)/g_a(0)$ which gives best agreement with R_γ is $9.8\pm0.7\pm0.3$, where the first error is the quadrature sum of statistical and systematic errors and the second error is due to the error in the experimental value of λ_{op}. This result for g_p is independent of both energy and time cuts as shown in Figs. 14 and 15. It is also relatively independent of λ_{op}, decreasing by $<5\%$ if the higher theoretical value of λ_{op} is used. However, it is 46% higher than the predicted value. Removing the Δ terms (f) and (g) of Fig. 1

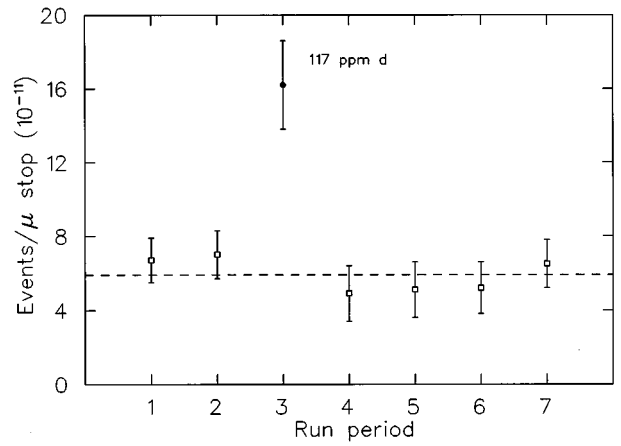

FIG. 16. Number of RMC events ($t>365$ ns, $E>60$ MeV) per muon stop versus run period. All run periods except number 3 had deuterium impurities of less than 2 ppm. The dashed line indicates the average of all deuterium-depleted runs.

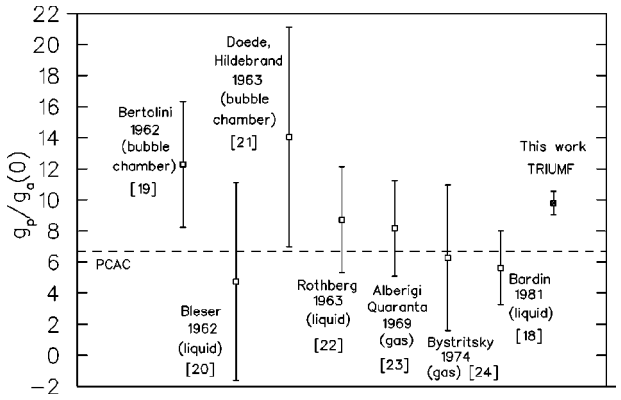

FIG. 17. The TRIUMF RMC value, from this work, of g_p/g_a compared to previous measurements [18–24] which use the ordinary muon capture reaction on ^{1}H. The dashed line indicates the predicted value of $g_p/g_a=6.7$.

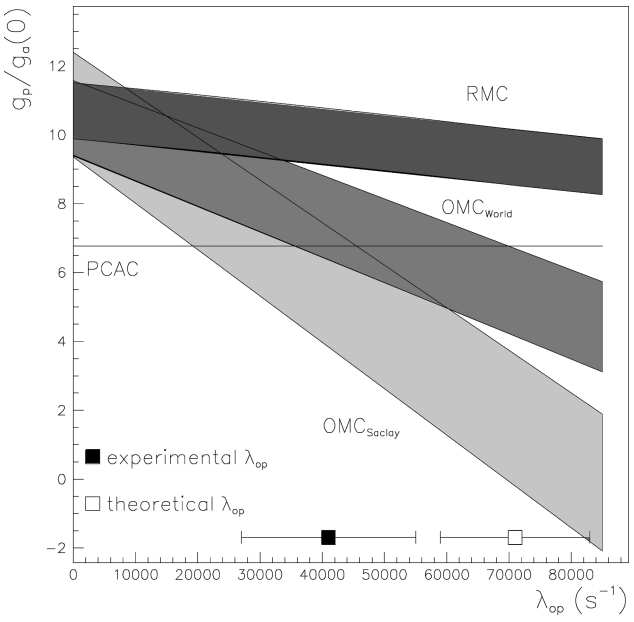

FIG. 18. $g_p(q^2)/g_a(0)$ evaluated at $q^2=-0.88m_\mu^2$, versus the ortho to para transition rate λ_{op} for OMC and RMC on hydrogen. The result of the present RMC experiment is shown by the dark-shaded band, the Saclay [18] result by the light-shaded band and the world average of OMC results by the medium-shaded band.

from Beder and Fearing's calculation has a small effect: from the measured branching ratio 2.10×10^{-8} the extracted value of g_p/g_a increases from 9.8 to 10.1. Earlier calculations of RMC on H [27,56] agree with Beder and Fearing to within 10%, which would seem to rule out differences in theory as the cause for the discrepancy.

Considering the complexity of the hyperfine structure of the $p\mu p$ ortho- and para-molecular states [30], and the fact that most of the capture goes through the ortho state, it is possible that some of the observed discrepancy in g_p/g_a may be due to the presence of bound vibrational excited states or uncertainty in the muon wave function overlap with the proton. However, the $p\mu p$ molecule has been investigated theoretically by many authors using a number of different calculational approaches [57–66]. The binding of the para ground state and the bindings and hyperfine structure of the ortho excited state appear to be well determined, and there are no other bound excited states. The muon wave function overlap with the proton (expressed by the so-called γ factors) is also well determined, indicating a negligible effect on the value of g_p/g_a extracted here.

The result from this experiment is compared to previous OMC results in Fig. 17. At the 1 σ level it is consistent with all other measurements except the Saclay [18] value. The world average of g_p/g_a measurements, 7.8 ± 1.4, is taken entirely from OMC experiments and includes the older bubble chamber data. It is dominated by the Saclay result which is the most recent and most precise OMC measurement. If the Saclay result were not included in the world average, the latter would have a very large uncertainty, a fact which motivated the present experiment. The present RMC result is 26% higher than the OMC world average value. Including the RMC result, the world average becomes 9.3 ± 0.7.

Figure 18 shows the dependence of RMC and OMC results on λ_{op}. The world average was derived from many experiments with widely different conditions and results. In particular the λ_{op} dependence is much larger for the Saclay data than for the present RMC or older OMC results because that group used a lifetime technique to measure the capture rate. The Saclay result agrees with the expected value of g_p only if the experimental value of λ_{op} is used. If the theoretical value of λ_{op} should be correct, the Saclay g_p would fall by about a factor of 3 and be far below the theoretical value.

In conclusion, the first measurement of the elementary RMC process is reported. At the 1 σ level the extracted g_p value is consistent with all previous measurements except one; however, its deviation from expectation is substantial. This is cause for concern because the prediction for the value of g_p is on firm theoretical ground; the chiral perturbation theory prediction has a precision of 3%. Provided that a large background has not eluded detection and that parameters used in the analysis are not grossly in error, some assumptions used in the calculation of R_γ from g_p need to be questioned. One of these is the pion pole dominance of the momentum dependence of the pseudoscalar form factor. For the range of momentum transfers accessible to RMC, deviations from the simple pole behavior are much more likely to be seen than they are in OMC. Another assumption to be questioned is whether a calculation based on tree level Feynman diagrams is adequate. Opat [27] anticipated a situation in which g_p measured using RMC would be higher than that measured with OMC. He cautioned that the calculation of multiple pion exchange terms may not have been properly handled. It is also possible that η and ρ exchanges need to be considered, although their contributions are expected to be small. Finally, it has been assumed throughout the foregoing analysis that the tensor form factor g_t is zero for momentum transfers typical of β decay, OMC and RMC. Its q^2 dependence is, in fact, unknown, so that it could possibly be small or zero for β decay and OMC, but large enough for RMC to explain some or all of the observed departure of g_p from the PCAC prediction.

Work in progress may shed light on this apparent discrepancy. New calculations of RMC on H are underway [67,68] which are based on chiral perturbation theory. A measure-

ment at TRIUMF of the ortho-to-para transition rate λ_{op} [69] will soon have results which may affect the value of g_p extracted from both the OMC and RMC experiments.

ACKNOWLEDGMENTS

The authors wish to thank the TRIUMF hydrogen target group, in particular A. Morgan and P. Burrill. Thanks also to G. Blaker of the TRIUMF RF group for keeping the rf separator running. We also thank A. Serna-Angel for his help in the construction of the drift chamber and W. Schott for his help with the data analysis. We are grateful to H. Fearing for access to his RMC computer code and many helpful discussions. One of us, T.v.E., wishes to thank the RMC group for their friendship and hospitality during his six month sabbatical at TRIUMF. This work was supported by the National Research Council and the Natural Sciences and Engineering Research Council (Canada), the National Science Foundation (USA), the Paul Scherrer Institute (Switzerland), and the Australia Research Council.

[1] G. Jonkmans *et al.*, Phys. Rev. Lett. **77**, 4512 (1996).
[2] S.C. McDonald, Ph.D. thesis, The University of Melbourne, 1994.
[3] G. Jonkmans, Ph.D. thesis, Université de Montréal, 1997.
[4] For example, L. Grenacs, Annu. Rev. Nucl. Part. Sci. **35**, 455 (1985), and references therein.
[5] N.C. Mukhopadhyay, Phys. Rep., Phys. Lett. **C30**, 1 (1977).
[6] M. Gell-Mann, Phys. Rev. **111**, 362 (1958).
[7] Y.K. Lee, L. Mo, and C.S. Wu, Phys. Rev. Lett. **10**, 253 (1963).
[8] M. Morita, Hyperfine Interact. **21**, 143 (1985).
[9] B.R. Holstein, Phys. Rev. C **29**, 623 (1984).
[10] Particle Data Group, R. M. Barnett *et al.* Phys. Rev. D **54**, 570 (1996), and references therein.
[11] A. Del Guerra, A. Giazotto, M.A. Giorgi, A. Stefanini, D.R. Botterill, H.E. Montgomery, P.R. Norton, and G. Matone, Nucl. Phys. **B107**, 65 (1976).
[12] A.S. Esaulov, A.M. Pilipenko, and Yu.I. Titov, Nucl. Phys. **B136**, 511 (1978).
[13] S. Choi *et al.*, Phys. Rev. Lett. **71**, 3927 (1993).
[14] L.A. Ahrens *et al.*, Phys. Lett. B **202**, 284 (1988).
[15] V. Bernard, N. Kaiser, and Ulf-G. Meissner, Phys. Rev. D **50**, 6899 (1994).
[16] S.L. Adler and Y. Dothan, Phys. Rev. **151**, 1267 (1966).
[17] L. Wolfenstein, *High-Energy Physics and Nuclear Structure*, edited by S. Devons (Plenum, New York, 1970), p. 661.
[18] G. Bardin, J. Duclos, A. Magnon, J. Martino, A. Richter, E. Zavattini, A. Bertin, M. Piccinini, and A. Vitale, Phys. Lett. **104B**, 320 (1981); G. Bardin, Ph.D. thesis, U. de Paris-Sud, Orsay, 1982.
[19] E. Bertolini, A. Citron, G. Gialanella, S. Focardi, A. Mukhin, C. Rubbia, and F. Saporetti, Proceedings of the International Conference on High Energy Physics, CERN, Geneva, 1962 (unpublished), p. 421; S. Focardi, G. Gialanella, C. Rubbia, and S. Saporetti, cited by C. Rubbia, in Proceedings of the International Conference on Fundamental Aspects of Weak Interactions, Brookhaven, 1963, Brookhaven National Laboratory Report No. BNL 837, 1964, p. 278.
[20] E.J. Bleser, L.M. Lederman, J.L. Rosen, J.E. Rothberg, and E. Zavattini, Phys. Rev. Lett. **8**, 288 (1962).
[21] J.H. Doede and R. Hildebrand, cited by C. Rubbia, in Proceedings of the International Conference on Fundamental Aspects of Weak Interactions [19], p. 277.
[22] J.E. Rothberg, E.W. Anderson, E.J. Bleser, L.M. Lederman, S.L. Meyer, J.L. Rosen, and I-T. Wang, Phys. Rev. **132**, 2664 (1963).
[23] A. Alberigi Quaranta, A. Bertin, G. Matone, F. Palmonari, G. Torelli, P. Dalpiaz, A. Placci, and E. Zavattini, Phys. Rev. **177**, 2118 (1969).
[24] V.M. Bystritsky, V.P. Dzhelepov, P.F. Ermolov, K.O. Oganesyan, M.N. Omel'yanenko, S.Yu. Porokhovoj, V.S. Roganov, A.I. Rudenko, and V.V. FIl'chenkov, Sov. Phys. JETP **39**, 19 (1974).
[25] D.S. Armstrong *et al.*, Phys. Rev. C **46**, 1094 (1992), and references therein.
[26] K. Huang, C.N. Yang, and T.D. Lee, Phys. Rev. **108**, 1340 (1957).
[27] G.I. Opat, Phys. Rev. **134**, B428 (1964), footnote 30.
[28] D.S. Beder and H.W. Fearing, Phys. Rev. D **35**, 2130 (1987).
[29] D.S. Beder and H.W. Fearing, Phys. Rev. D **39**, 3493 (1989).
[30] D.D. Bakalov, M.P. Faifman, L.I. Ponomarev, and S.I. Vinitsky, Nucl. Phys. **A384**, 302 (1982); L. Ponomarev, in *Muonic Atoms and Molecules*, edited by L. A. Schaller and C. Petitjean (Birkhauser Verlag, Basel 1993).
[31] N.M.M. Al-Qazzaz *et al.*, Nucl. Instrum. Methods **174**, 35 (1980).
[32] E.W. Blackmore *et al.*, Nucl. Instrum. Methods Phys. Res. A **234**, 235 (1985).
[33] W. Bertl, D. Healey, J. Zmeskal, M.D. Hasinoff, M. Blecher, and D.H. Wright, Nucl. Instrum. Methods Phys. Res. A **355**, 230 (1995).
[34] D.H. Wright *et al.*, Nucl. Instrum. Methods Phys. Res. A **320**, 249 (1992).
[35] P. Bennett, M. Blecher, R. Chan, S. Daviel, M. Hasinoff, S. Ko, R. Poutissou, D. Sample, and D. Wright, IEEE Trans. Nucl. Sci. **NS37**, 1200 (1990).
[36] T. Suzuki, D.F. Measday, and J.P. Roalsvig, Phys. Rev. C **35**, 2212 (1987).
[37] G. Bardin, J. Duclos, A. Magnon, J. Martino, A. Richter, E. Zavattini, A. Bertin, M. Piccinini, A. Vitale, and D. Measday, Nucl. Phys. **A352**, 365 (1981).
[38] Particle Data Group, R. M. Barnett *et al.* Phys. Rev. D **54**, 123 (1996), and references therein.
[39] Metabolic Systems Inc., Acton, MA, 01720.
[40] Department of Earth Sciences, University of Waterloo, Waterloo, Ontario, Canada N2L 3G1.
[41] E.J. Bleser, E.W. Anderson, L.M. Lederman, S.L. Meyer, J.L. Rosen, J.E. Rothberg, and I-T. Wang, Phys. Rev. **132**, 2679 (1963).
[42] G. Conforto, C. Rubbia, E. Zavattini, and S. Focardi, Nuovo Cimento **33**, 1001 (1964).
[43] Yu.G. Budyashov, P.F. Ermolov, A.D. Konin, A.I. Mukhin, K.O. Oganesyan, and V.G. Zinov, Dubna, JINR Report No. P15, 1968, p. 3964.

[44] V.M. Bystritsky *et al.*, Sov. Phys. JETP **40**, 606 (1976).
[45] V.M. Bystritsky *et al.*, JINR Report No. E1, 1975, p. 8881.
[46] V.P. Dzehelepov, P.F. Ermolov, E.A. Kushnirenko, V.I. Moskalev, and S.S. Gershtein, Sov. Phys. JETP **15**, 306 (1962).
[47] A. Bertin, M. Bruno, A. Vitale, A. Placci, and E. Zavattini, Lett. Nuovo Cimento **4**, 449 (1972).
[48] I-T. Wang, E.W. Anderson, E.J. Bleser, L.M. Lederman, S.L. Meyer, J.L. Rosen, and J.E. Rothberg, Phys. Rev. **139B**, 1528 (1965).
[49] L.B. Auerbach, R.J. Esterling, R.E. Hill, D.A. Jenkins, J.T. Lach, and N.H. Lipman, Phys. Rev. **138B**, 127 (1965).
[50] H.W. Fearing, Phys. Rev. C **21**, 1951 (1980).
[51] P. Hänggi, R.D. Viollier, U. Raff, and K. Alder, Phys. Lett. **51B**, 119 (1974).
[52] F. Herzog and K. Alder, Helv. Phys. Acta **53**, 53 (1980).
[53] P. Kitching, REVMOC, TRIUMF internal Report No. TRI-71-2, 1971; G. Stinson and P. Kitching, Modifications to the Computer Program REVMOC, TRIUMF internal Report No. TRI-DNA-73-4, 1973; C. Kost and P. Reeve, Proceedings of Computing in Accelerator Design and Operation Conference, Berlin, 1983 (unpublished), p. 158.
[54] GEANT Version 3.21, CERN, Geneva, 1993.
[55] F. Mulhauser *et al.*, Phys. Rev. A **53**, 3069 (1996).
[56] M. Gmitro and A.A. Ovchinnikova, Nucl. Phys. **A356**, 323 (1981).
[57] M.P. Faifman, Muon Catal. Fusion **4**, 341 (1989).
[58] D.D. Bakalov *et al.*, Nucl. Phys. **A384**, 302 (1982).
[59] Ya.B. Zel'dovich and S.S. Gerstein, Sov. Phys. Usp. **3**, 593 (1961).
[60] I.I. Ponomarev and M.P. Faifman, Sov. Phys. JETP **44**, 886 (1976).
[61] S. Weinberg, Phys. Rev. Lett. **4**, 575 (1960).
[62] W.R. Wessel and P. Phillipson, Phys. Rev. Lett. **13**, 23 (1964).
[63] A. Halpern, Phys. Rev. Lett. **13**, 660 (1964).
[64] S.I. Vinitskii *et al.*, Sov. Phys. JETP **52**, 353 (1980).
[65] D.D. Bakalov and S.I. Vinitskii, Sov. J. Nucl. Phys. **372**, 372 (1980).
[66] D.D. Bakalov, S.I. Vinitskii, and V.S. Melezhik, Sov. Phys. JETP **52**, 820 (1980).
[67] K. Kubodera (private communication).
[68] H.W. Fearing (private communication).
[69] D.S. Armstrong and T.P. Gorringe, TRIUMF Experiment No. 766, 1996.